Spatial mapping of integrin interactions and dynamics during cell migration by Image Correlation Microscopy

Paul W. Wiseman[1,*], Claire M. Brown[2,*,‡], Donna J. Webb[2], Benedict Hebert[1], Natalie L. Johnson[2], Jeff A. Squier[3], Mark H. Ellisman[4] and A. F. Horwitz[2]

[1]Departments of Chemistry and Physics, McGill University, 801 Sherbrooke St. W. Montreal, Quebec H3A 2K6, Canada
[2]Department of Cell Biology, University of Virginia, PO Box 800732, Charlottesville, VA 22908, USA
[3]Department of Physics, Colorado School of Mines, 1523 Illinois Street, Golden, CO 80401, USA
[4]Departments of Neurosciences and Bioengineering, and National Center for Microscopy and Imaging Research, University of California, San Diego, CA 92093, USA

*These authors contributed equally to this work
‡Author for correspondence (e-mail: cmb8t@virginia.edu)

Accepted 21 July 2004
Journal of Cell Science 117, 5521-5534 Published by The Company of Biologists 2004
doi:10.1242/jcs.01416

Summary

Image correlation microscopy methodology was extended and used to determine retrospectively the density, dynamics and interactions of α5-integrin in migrating cells. α5-integrin is present in submicroscopic clusters containing 3-4 integrins before it is discernibly organized. The integrin in nascent adhesions, as identified by the presence of paxillin, is ~1.4 times more concentrated, ~4.5 times more clustered and much less mobile than in surrounding regions. Thus, while integrins are clustered throughout the cell, they differ in nascent adhesions and appear to initiate adhesion formation, despite their lack of visible organization. In more mature adhesions where the integrin is visibly organized there are ~900 integrins μm^{-2} (about fivefold higher than surrounding regions). Interestingly, α5-integrin and α-actinin, but not paxillin, reside in a complex throughout the cell, where they diffuse and flow together, even in regions where they are not organized. During adhesion disassembly some integrins diffuse away slowly, α-actinin undergoes a directed movement at speeds similar to actin retrograde flow (0.29 μm min^{-1}), while all of the paxillin diffuses away rapidly.

http://jcs.biologists.org/cgi/content/full/117/23/5521/DC1

Key words: α5-integrin, Cell migration, Adhesions, α-actinin, Paxillin, Correlation microscopy, Cytoskeleton

Introduction

During migration, the cell executes and integrates a cycle of activities that include the formation of a membrane protrusion and the assembly of adhesion complexes at the leading edge, the forward movement of the cell body, and detachment of adhesions and retraction at the cell rear (Horwitz and Parsons, 1999; Lauffenburger and Horwitz, 1996). These processes repeat cyclically allowing the cell to move forward continuously. The spatial segregation of these activities implies molecular heterogeneities and a polarity that are intrinsic to a migrating cell (Ridley et al., 2003). It also suggests the existence of mechanisms that maintain this polarity during migration. The implication is that the molecules that mediate migration-related processes have different concentrations, dynamics and/or intermolecular interactions across the cell (Webb et al., 2002; Del Pozo et al., 2002). While some localized sites of activities, such as mature adhesions, can be readily visualized by optical microscopy, even these are not readily visualized in some of the most rapidly migrating cells.

The complex and dynamic macromolecular choreography performed by migrating cells has led to the recognition that novel physico-chemical methods will be required to understand this molecular process (Webb et al., 2003). The emergence of quantitative, fluorescence-based microscopy techniques like fluorescence correlation spectroscopy (FCS), fluorescence recovery after photobleaching (FRAP) and speckle microscopy promise to provide the methodology to dissect molecular mechanisms of complex spatially and temporally regulated processes like cell migration and provide the quantitative data needed to model them (for a review, see Webb et al., 2003). These tools allow concentrations, intermolecular interactions, transport properties and dynamics of biomolecules to be determined in situ. Thus, they provide the information required for understanding the mechanisms of adhesion and signaling dynamics that underlie the complex process of cell migration.

In this study we have developed and extended image correlation microscopy [ICM – also known as image correlation spectroscopy (ICS) (Petersen et al., 1993; Petersen et al., 1998; Wiseman and Petersen, 1999; Wiseman et al., 2000)], a variant of FCS, to investigate the heterogeneities in the distribution, dynamics and interactions of α5-integrin and α-actinin in the context of the formation and disassembly of adhesions during cell migration. While ICM has been used previously on static images, we have extended the technology and developed methods to analyze image stacks retrospectively from time-lapse sequences to produce cellular maps of molecular densities, interactions, diffusion rates, and the net direction and magnitude of non-random, concerted molecular movement. Using these maps we have examined specific areas of migrating cells before, during and after events such as protrusion formation and adhesion formation and disassembly. These analyses revealed several novel observations including

the clustering of integrins in newly forming adhesions, differences in the transport properties of integrin, paxillin and α-actinin in regions where adhesions are disassembling, and a novel, robust interaction between integrin and α-actinin, but not paxillin, outside of adhesions.

Materials and Methods

Cell culture

CHO-K1, CHO-B2 (a cell line deficient in expression of α5-integrin) (Schreiner et al., 1991) and MEF cell lines were cultured in minimum essential medium (MEM) supplemented with 10% FBS, and glutamine, as well as 0.5 mg ml^{-1} neomycin (G418) when they were expressing fusion proteins. Nonessential amino acids were also added to the CHO media. Cells were maintained in a humidified, 8.5% CO_2 atmosphere at 37°C. Cells were lifted with trypsin and plated on 40 mm diameter No. 1.5 coverslips or on home-made 35 mm glass bottomed dishes coated with an integrin-activating (2, 5 or 10 μg ml^{-1} fibronectin FN) or non-integrin-activating matrix (200 μg ml^{-1} poly-D-lysine). Cells were maintained in CCM1 medium (HyClone, Logan, UT) at 37°C during imaging with a Bioptechs FCS2 closed incubation chamber, or a Warner Instruments heated stage insert (Bioptechs, Butler, PA; Warner Instruments, Hamden, CT), in combination with a Bioptechs objective heater. Nontransfected CHO cells were used as control samples to determine autofluorescence background levels. Cell samples that had been fixed with 4% paraformaldehyde in PBS for 20 minutes at room temperature were also prepared and imaged to provide a control for any contributions from mechanical vibrations, stage translations and laser fluctuations. Stable CHO-B2 α5-GFP-expressing cells, plasmids for α5-GFP, α-actinin-GFP and paxillin-GFP, and transfection protocols are explained in detail by Laukaitis et al. and Webb et al. (Laukaitis et al., 2001; Webb et al., 2004).

Single-photon confocal microscopy

Confocal images were collected on an Olympus Fluoview 300 microscope with an IX70 inverted microscope fitted with a 60× PlanApo (1.40 NA) oil immersion objective. Excitation was from the 488 nm laser line of a 40 mW Ar ion laser (Melles Griot, Tokyo, Japan) attenuated to 0.1-0.2% power using an acoustic optic tunable filter. A Q500LP dichroic mirror was used for the laser excitation and for collection of the emission from GFP-labeled cells. Images were collected using the Fluoview software with either 800×600 pixels at 3× zoom or 1024×1024 pixels at 10× zoom corresponding to a pixel resolution of 0.111 μm or 0.023 μm with the slow scan speed.

Two-photon microscopy

Multi-photon imaging was conducted using a Biorad RTS2000MP video rate capable two-photon/confocal microscope (BioRad, Hertfordshire, UK) in inverted configuration, coupled with a MaiTai pulsed femtosecond Ti:sapphire laser (Spectra Physics, Mountain View, CA) tunable from 780-920 nm. The microscope uses a resonant galvanometer mirror to scan horizontally at the NTSC line scan rate. Aspects of the microscope scan optics and electronics have been described in more detail previously for a prototype microscope of similar configuration (Fan et al., 1999). Point detection is employed using a photomultiplier tube(s) with a fully open confocal pinhole(s) when imaging. For GFP the laser was tuned to 890 nm and a 560 DCLPXR dichroic mirror and an HQ528/50 emission filter were employed for light detection. For imaging cells expressing both CFP and YFP fusion proteins the laser was tuned to 880 nm and a D500LP dichroic mirror, and HQ485/22 and HQ560/40 emission filters were used for detection and separation of emitted light. All laser filters were from Chroma Technology Co. (Brattleboro, VT).

Image time series were collected using a PlanApo Nikon 60× oil immersion objective lens (NA 1.40), which was mounted in an inverted configuration. Images having dimensions of 480 by 512 pixels were typically collected with an optical zoom setting of 2× giving 0.118 μm per pixel. Individual image frames sampled from the cells were accumulated as averages of 32 video rate scans.

Image autocorrelation and cross-correlation analysis

Microscope image time series volumes were viewed, and image sections of 32^2, 64^2, 128^2 or 256^2 pixels were selected from regions of the cell and exported for image correlation analysis using a custom C++ program written for the PC. Correlation calculations for all image time series and nonlinear least squares fitting of the spatial correlation functions were performed in a LINUX environment on a 1.2 GHz dual processor PC using programs written in FORTRAN. Discrete intensity fluctuation autocorrelation functions were calculated from the image sections as has been previously described (Wiseman et al., 2000). Nonlinear least squares fitting to the calculated temporal correlation functions was done on a PC using Sigma Plot for Windows (SPSS, Chicago IL). The equations used for the calculation and fitting of the normalized intensity fluctuation autocorrelation and cross-correlation functions (both spatial and temporal) are described below.

Intensity correction for GAP-GFP experiments

The original GAP-GFP experiments were done on cells expressing GFP (S65A), thus the data had to be corrected for differences between the brightness of EGFP and GFP (S65A). Comparisons were made by ICM and also by a molecular brightness analysis. Both measurements show that the EGFP was found to be 1.4× brighter than the GFP (S65A) so the data was corrected accordingly.

Theory

In the present work we present a general framework of the theory for image correlation analysis and introduce equations new to the analysis in this report. For a more complete introduction see Wiseman et al. (Wiseman et al., 2000).

Generalized spatio-temporal correlation function

We define a generalized spatio-temporal correlation function which is a function of spatial lag variables ξ and η and of a temporal lag variable τ for detection channels a and b:

$$r_{ab}(\xi,\eta,\tau) = \frac{\langle \delta i_a(x,y,t)\delta i_b(x+\xi,y+\eta,t+\tau)\rangle}{\langle i_a\rangle_t\langle i_b\rangle_{t+\tau}}, \quad (1)$$

where the spatial intensity fluctuations are defined as:

$$\delta i_a(x,y,t) = i_a(x,y,t) - \langle i_a\rangle_t, \quad (2)$$

where $\langle i_a\rangle_t$ is the average intensity of the image collected in detection channel a at time t in the image series. In cases where a=b=1 or a=b=2, Eq. 1 defines a normalized intensity fluctuation autocorrelation function for detection channel 1 or 2 (Fig. S1A). When a=1 and b=2, Eq. 1 represents a normalized intensity fluctuation cross-correlation function between the two detection channels. The angular brackets indicate an ensemble average.

Spatial autocorrelation and cross-correlation

For a fixed collection time t (i.e. for one image) a normalized spatial intensity fluctuation autocorrelation function (a=b=1 or 2) or cross-correlation function (a=1 and b=2) may be defined by evaluating Eq. 1 with zero time lag:

$$r_{ab}(\xi,\eta,0)_t = \frac{\langle \delta i_a(x,y,t)\delta i_b(x+\xi,y+\eta,t)\rangle}{\langle i_a\rangle_t\langle i_b\rangle_t}. \quad (3)$$

We calculate the discrete approximation to these spatial correlation functions by Fourier methods and fit them with Gaussian functions by nonlinear least squares methods as has been described previously (Petersen et al., 1993; Wiseman and Petersen, 1999). The generalized Gaussian fit function is represented as follows (note in this fitting equation and those that follow, the fit parameters are highlighted in bold type):

2D Spatial Correlation Function

$$r_{ab}(\xi,\eta,0)_n = \mathbf{g_{ab}(0,0,0)_n} \exp - \left\{ \frac{\xi^2+\eta^2}{\mathbf{\omega^2_{2p\ ab}}} \right\} + \mathbf{g_{\infty\ abn}}\ , \quad (4)$$

where the subscript n denotes spatial correlation functions or fit parameters obtained for a particular image number n (or from a pair of images in the two detection channels for spatial cross-correlation) in the time series. We obtain best fit estimates of the zero spatial lag correlation function amplitude [$g_{ab}(0,0,0)_n$], the e^{-2} correlation radius in the focal plane ($\omega_{2p\ ab}$) and fitting offset parameter at long correlation lengths ($g_{\infty\ abn}$) (Petersen et al., 1993). We have adopted a new notation using an infinity symbol for the offset parameter because it emphasizes the fact that it is for incomplete decay at long correlation lengths and times (see Eqs 11, 12 and 13), and is less likely to be confused with the zero lag correlation function amplitude. Note also that ω_{2p}, the effective two-photon e^{-2} correlation radius, is proportional to the e^{-2} beam radius (ω_o) for the laser fundamental wavelength divided by square root of two.

We calculated the degree of aggregation (DA) as the product of the spatial autocorrelation function amplitude and the mean intensity for each image.

$$DA = g_{aa}(0,0,0)_n \langle i \rangle_n\ . \quad (5)$$

A time series plot of the DA parameter reflects the relative changes in the mean aggregate size (Petersen, 1986; Wiseman and Petersen, 1999).

Temporal autocorrelation and cross-correlation

A normalized temporal intensity fluctuation autocorrelation function (a=b=1 or 2) or cross-correlation function (a=1 and b=2) may be defined by evaluating Eq. 1 with zero spatial lags (Fig. S1B):

$$r_{ab}(0,0,\tau) = \frac{\langle \delta i_a(x,y,t)\delta i_b(x,y,t+\tau)\rangle}{\langle i_a\rangle_t \langle i_b\rangle_{t+\tau}}\ . \quad (6)$$

The decay of this function is related to the temporal persistence of the average spatial correlation between images in the time series that are separated by time lag τ. The shapes and decay rates of the temporal correlation functions are dependent on the dynamic transport properties of the independent discrete fluorescent units that contribute to intensity fluctuations on the time scale of the measurement. The temporal correlation functions can be solved analytically for the decay functions that characterize diffusive or flow molecular transport in a two-dimensional (2D) system (Thompson, 1991). For a multi-component system illuminated by a focused laser beam in TEM_{00} mode, the temporal correlation function decay will have the following form:

$$g(\tau) = \frac{\sum_{i=1}^{R} \alpha_i^2 \langle N_i\rangle M_i}{\left\{ \sum_{i=1}^{R} \alpha_i \langle N_i\rangle \right\}^2}\ , \quad (7)$$

where α_i is the ratio of the fluorescent yield of species i relative to that of the monomer subunit ($\alpha_i = Q_i/Q_1$), M_i is a general fluctuation relaxation factor specific for each mode of transport and the summation is performed over all fluorescent species (Thompson, 1991). The analytical form of the fluctuation relaxation factor for 2D diffusion is:

$$M_i = \left(1 + \frac{\tau}{\tau_d} \right)^{-1}\ , \quad (8)$$

while for 2D flow it is:

$$M_i = \exp - \left(\frac{\tau}{\tau_f} \right)^2\ , \quad (9)$$

and for a diffusing species with a biased flow direction it takes the form:

$$M_i = \left(1 + \frac{\tau}{\tau_d} \right)^{-1} \exp \left\{ - \left(\frac{\tau}{\tau_f} \right)^2 \left(1 + \frac{\tau}{\tau_d} \right)^{-1} \right\}. \quad (10)$$

Note that τ_d and τ_f are the characteristic diffusion and flow times for fluctuations associated with the two transport modes.

Temporal autocorrelation functions were calculated for selected image series sections and were fit with three separate functional forms that are analytical solutions for the generalized intensity fluctuation correlation function appropriate for specific cases of 2D transport phenomena. The fit functions for 2D diffusion, combined 2D diffusion and flow for a single population of molecules, and two populations separately flowing and diffusing in 2D, were calculated for each temporal correlation function and the appropriate functional form selected based on the highest R^2 correlation coefficient for the fits. The fit functions applied were:

2D diffusion (Fig. S1C,E):

$$r_{ab}(0,0,\tau) = \mathbf{g_{ab}(0,0,0)} \left(1 + \frac{\tau}{\mathbf{\tau_d}} \right)^{-1} + \mathbf{g_{\infty\ ab}}\ , \quad (11)$$

2D diffusion and flow for a single population (Fig. S1D):

$$r_{ab}(0,0,\tau) = \mathbf{g_{ab}(0,0,0)} \left(1 + \frac{\tau}{\mathbf{\tau_d}} \right)^{-1} \exp \left\{ - \left(\frac{|\mathbf{v_f}|\tau}{\langle \omega_{2p\ ab} \rangle} \right)^2 \left(1 + \frac{\tau}{\mathbf{\tau_d}} \right)^{-1} \right\} + \mathbf{g_{\infty\ ab}}\ , \quad (12)$$

2D diffusion and flow for two populations (i=1, 2) (Fig. S1F):

$$r_{ab}(0,0,\tau) = \mathbf{g_{ab}(0,0,0)_1} \left(1 + \frac{\tau}{\mathbf{\tau_{d1}}} \right)^{-1} + \mathbf{g_{ab}(0,0,0)_2} \exp \left\{ - \left(\frac{|\mathbf{v_{f2}}|\tau}{\langle \omega_{2p\ ab} \rangle} \right)^2 \right\} + \mathbf{g_{\infty\ ab}}\ , \quad (13)$$

where the fit parameters highlighted in bold type are the zero time lag correlation amplitude [$g_{ab}(0,0,0)$], the characteristic diffusion time (τ_d), the mean flow speed ($|v|_f$) and an offset parameter for the correlation function at long correlation times ($g_{\infty\ ab}$). The $<\omega_{2p\ ab}>$ value is the mean lateral e^{-2} correlation radius obtained by averaging the $\omega_{2p\ ab}$ values obtained by fitting of the individual spatial correlation functions for each image in the time series using Eq. 4.

Diffusion coefficients were calculated using the best fit lateral

correlation radius and the characteristic diffusion time (Elson and Magde, 1974):

$$D_{exp} = \frac{\langle \omega_{2p\,ab} \rangle^2}{4\tau_d} . \quad (14)$$

The nonlinear least squares fitting yields best fit parameters for the characteristic diffusion time, τ_d, and the mean flow speed, $|v_f|$, for the single population. Note that the characteristic flow time, τ_f, is inversely proportional to the mean flow speed:

$$\tau_f = \frac{\langle \omega_{2p\,ab} \rangle}{|v_f|} . \quad (15)$$

For analysis of the single photon CLSM data, ω_{2p} is simply replaced by the e^{-2} radius at the focus (ω_o) for the excitation laser. For the two population fits (Eq. 13), the separate zero lag amplitudes are interpreted according to a variant of Eq. 7 evaluated at zero time lag:

$$g_{ab}(0,0,0)_i = \frac{\alpha_i^2 \langle N_i \rangle}{\{\alpha_1 \langle N_1 \rangle + \alpha_2 \langle N_2 \rangle\}^2} , \text{ where } i = 1 \text{ or } 2 . \quad (16)$$

Estimates of the fraction of immobile species for each correlation measurement were obtained from the zero time lag fit values and the long correlation time offset fit value. By assuming that the immobile species have the same aggregation state as the mobile species, we can calculate the percent of immobile species in the following way (E. Feinstein et al., unpublished):

$$\%\ \text{Immobile} = \frac{\mathbf{g_{\infty\,ab}}}{\mathbf{g_{\infty\,ab}} + \sum_{i=1}^{R} \mathbf{g_{ab}(0,0,0)_i}} \cdot 100 , \quad (17)$$

where the summation runs over the number of distinct mobile populations detected (either one or two for the current studies).

Estimates of the change in DA for only the adhesive areas of the region of interest were calculated using the following relationship:

$$DA_t\langle i_t \rangle = DA_a\langle i \rangle_a + DA_{na}\langle i \rangle_{na} . \quad (18)$$

The subscripts t, a and na correspond to total (measured value), adhesive (a) and nonadhesive (na) regions. The area of each population is included in the average intensity terms which are multiplied by the percent area each population takes up in the image. For calculations of the number of integrins per adhesion the DA from nonadhesive regions of cells (without paxillin containing adhesions) were used as DA_{na}, and it was assumed that the change in DA is due primarily to changes in the adhesive areas and not adjacent nonadhesive areas.

Image correlation velocity mapping

Image sections that had temporal autocorrelation functions best fit with a flow component were selected for further correlation analysis to obtain velocity maps. A full space-time autocorrelation function was calculated from the image series taking into account non-zero spatial lags and temporal lags (effectively a complete discrete calculation of Eq. 1). We resolved the spatial correlation peaks for flowing and diffusing components which would separate at longer temporal lags (Fig. S1G). Velocity components in x and y for the flowing components were obtained by fitting the trajectory of the spatial correlation peak for the flowing population (B.H. and P.W.W., unpublished).

Cross-talk correction for cross-correlation

Control experiments with cells only transfected with CFP or YFP showed that there was ~9% signal bleed through from the cyan channel into the yellow channel but virtually no bleed through (<1%) from the yellow channel into the cyan for the two-photon microscopy imaging. Signal cross-talk from channel 1 (CFP) into channel 2 (YFP) will systematically affect both the autocorrelation of the YFP signal and the cross-correlation between the two channels. However, under these conditions (cross-talk from channel 1 into 2), the cross-talk contribution will be a fractional contribution of the autocorrelation of the first channel:

$$r_{bb}(\xi,\eta,\tau) = \frac{\langle \delta i_2(x,y,t)\delta i_2(x+\xi,y+\eta,t+\tau)\rangle + \gamma^2\langle \delta i_1(x,y,t)\delta i_1(x+\xi,y+\eta,t+\tau)\rangle}{[\langle i_2\rangle + \gamma\langle i_1\rangle]^2} , \quad (19)$$

$$r_{ab}(\xi,\eta,\tau) = \frac{\langle \delta i_1(x,y,t)\delta i_2(x+\xi,y+\eta,t+\tau)\rangle + \gamma\langle \delta i_1(x,y,t)\delta i_1(x+\xi,y+\eta,t+\tau)\rangle}{\langle i_1\rangle[\langle i_2\rangle + \gamma\langle i_1\rangle]} , \quad (20)$$

where γ is the fraction of cross-talk from channel 1 into channel 2. For the two color ICCS experiments, we completely corrected the cross-correlation functions and the channel 2 autocorrelation functions for the cross-talk contribution from channel 1.

Results

ICM reveals the presence of submicroscopic clusters of α5-integrin

The prominent adhesions that characterize quiescent, highly adherent cells growing on rigid, planar substrates have been studied extensively. However, many cells, including some of the most motile cells in vitro and those migrating in vivo, do not generally show highly organized adhesions. In addition, during adhesion formation some components are present initially but are not discernibly organized when viewed with the light microscope (Laukaitis et al., 2001). For example, new adhesions in protrusions contain organized paxillin (Fig. 1A-D) before α5-integrin is visibly clustered (Fig. 1E-H).

ICM was used to characterize the submicroscopic organization of α5-integrin. In ICM the spatial variations in fluorescence intensity are used to compute the number of fluorescent molecules and their degree of aggregation (Petersen et al., 1998; Wiseman et al., 2000). In this analysis, either an individual molecule or an independent aggregate is scored as a single fluorescence entity contributing to the measured average number of fluorescent entities, <N>, within the laser beam focus. For our analyses, GAP-GFP (a 20 amino acid membrane targeting sequence from GAP-43 that contains two palmitoylated cysteine residues) (Liu et al., 1993) was used to calibrate the relationship between <N>, as measured by ICM, and the fluorescence intensity of a single GFP fluorophore (Fig. 2A). This allowed the determination of the absolute number of individual molecules in regions of the cell and their degree of aggregation (DA, Eq. 5). As expected, there was a linear relation between the intensity of GAP-GFP fluorescence and the number of fluorescent entities as determined by ICM analyses on cells of varying expression levels. The calculated DA for GAP-GFP was constant despite an order of magnitude range of expression levels, showing that the GAP-GFP is not aggregated even at higher expression levels. This was confirmed by an ICM analysis of a mutant GFP, in which the low affinity GFP aggregation site had been mutated (Zacharias et al., 2002).

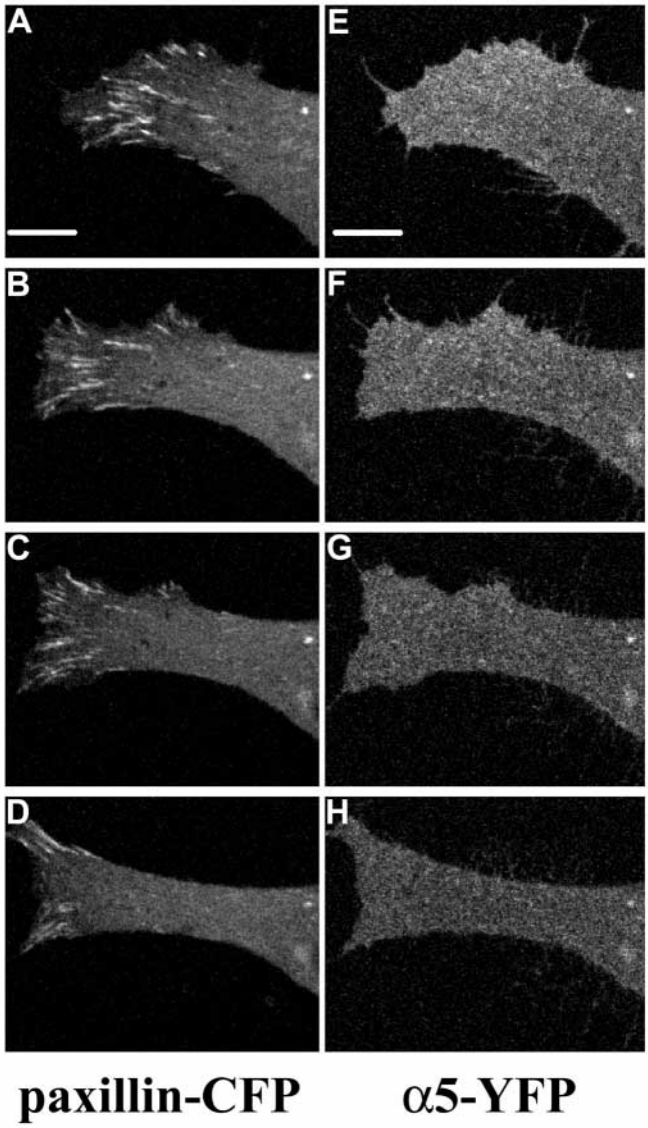

Fig. 1. Cells expressing both paxillin-CFP and α5-YFP show visibly organized paxillin but not α5-integrin. (A-D) Expressed paxillin-CFP in a protrusion at various time points of a confocal image time series of MEF cells during adhesion formation and turnover. The pairwise corresponding images of α5-YFP expression for the same regions of the cell are shown in E-H. Cells were 24 hours post-transfection and were plated on 1 μg ml^{-1} fibronectin for an hour before imaging at 37°C. Scale bar, 10 μm.

CHO-B2 cells – which are α5-integrin deficient, do not adhere to fibronectin, and contain few other integrins (Schreiner et al., 1991) – expressing variable levels of α5-integrin were plated on either 200 μg ml^{-1} poly-D-lysine or 2 μg ml^{-1} fibronectin (Fig. 2B,C, respectively). The DA for α5-integrin in cells plated on poly-D-lysine is virtually identical to that for GAP-GFP, showing that it is not clustered. The DA for α5-integrin on cells plated on fibronectin is, by contrast, about three times greater than that for GAP-GFP depending on the expression level. The degree of aggregation was lower in cells expressing higher levels of integrin, e.g. 2.3 vs 3.5 (Fig. 2D), suggesting that the size and number of integrin clusters are relatively constant. This aggregation could arise from either cytoplasmic influences or from heterogeneities in the matrix. On the basis of the intensity calibrated ICM data and a measured average CHO cell area of 2500 μm^2 (from DIC images), we estimate that the number of integrins in the cells used for these experiments ranged from $1\text{-}30\times10^5$ integrins per cell. For comparison, fibroblasts have approximately 5×10^5 integrins per cell (Neff et al., 1982). In control experiments, 60% of the unlabeled CHO K1 cells showed no discernable correlation function. Of the images that produced correlation functions the number densities and fluorescence intensities were no more than 4% of the typical values measured for α5-GFP.

α5-integrin is concentrated and clustered in nascent adhesions

We have previously reported that paxillin is organized before α5-integrin in dynamic, nascent adhesions (Laukaitis et al., 2001), leading to a working hypothesis that nascent adhesions are nucleated by relatively small, subresolution integrin clusters. To test this hypothesis, we used intensity analysis combined with ICM to examine the organization of integrins inside and outside of nascent adhesions. CHO B2 cells or MEFs were doubly transfected with paxillin-CFP and α5-YFP. The intensity of α5-integrin-YFP (Fig. 3B) was measured under adhesions identified by the presence of organized paxillin-CFP in protruding regions of the cell (Fig. 3A) and compared with intensities in areas adjacent to these adhesions. On average there was a 35% increase in the density of integrin under nascent, paxillin containing adhesions, with the increase ranging from 5% to over 90% (Fig. 3C). A similar increase in density was not seen with the GAP-GFP membrane marker. When these data were sorted and binned by the average intensity of integrin on each cell, the highest relative density of integrins in adhesions occured on cells expressing lower amounts of integrin (Fig. 3D). This is consistent with the notion that the number of sequestered integrins in adhesions is relatively fixed, at least at this stage of adhesion maturation.

The average DA for α5-integrin is 1.6±0.2 times higher in regions that contain organized paxillin, indicating that integrins are also more clustered in regions containing adhesions. When these data were normalized for the fraction of area in the analyzed regions actually occupied by adhesions (Eq. 18) and the average increase in integrin concentration in the adhesions, the increase in the DA in nascent adhesions was actually 4.5±0.6 times higher than that in nonadhesive regions. Therefore, α5-integrin is not only more concentrated in nascent adhesions, but it is also more clustered there. A FRAP analysis of the integrin under the nascent adhesions, as revealed by the presence of organized paxillin, revealed that it is more immobile (32%; Fig. 4D,F, open triangles) compared with surrounding regions (0%; Fig. 4F, filled circles) and not as immobile as mature adhesions (61%; Fig. 4A-C,E, open triangles). Taken together, these data are all consistent with the hypothesis that new adhesions are nucleated by relatively small, submicroscopic integrin clusters.

Dynamics of α5-integrin

The disassembly of adhesions is thought to result in a transient, local concentration of adhesion molecules that arises from a

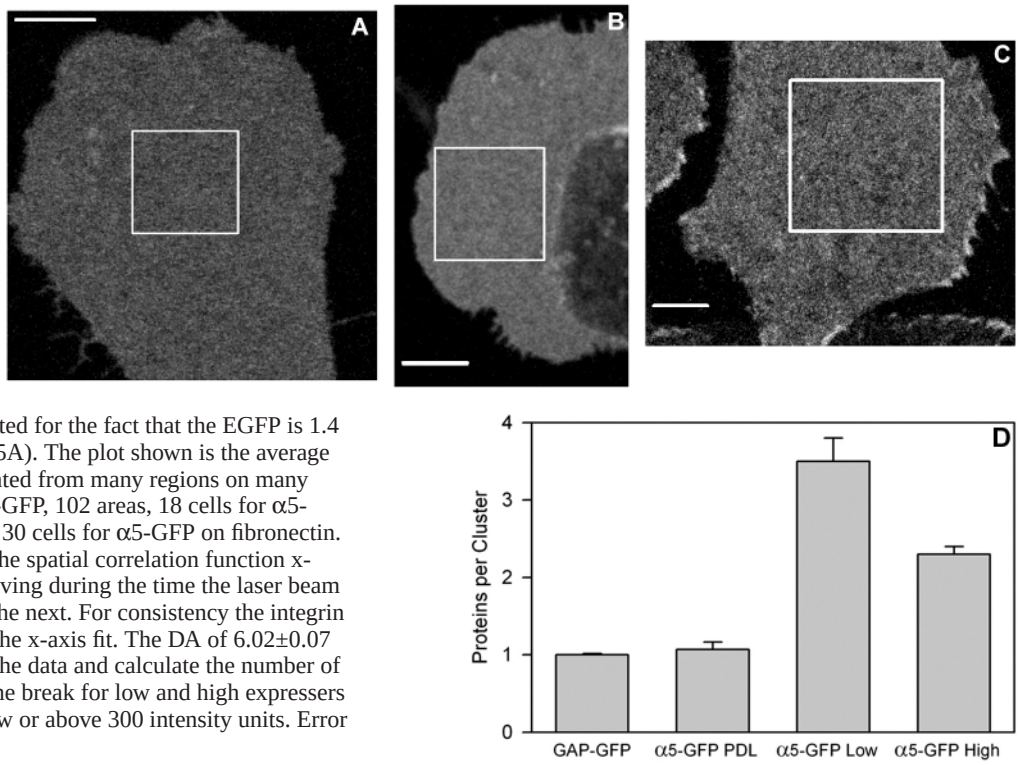

Fig. 2. Average cluster size for α5-integrin in CHO B2 cells. Confocal images of a CHO K1 cell expressing GAP-GFP and plated on coverslips coated with 2 μg ml^{-1} fibronectin (A), or CHO B2 cells expressing α5-GFP plated on coverslips coated with either 200 μg ml^{-1} poly-D-lysine (B) or 2 μg ml^{-1} fibronectin (C). Data were corrected for the fact that the EGFP is 1.4 times brighter than the GAP-GFP (S65A). The plot shown is the average number of integrins per cluster calculated from many regions on many cells (D), 166 areas, 44 cells for GAP-GFP, 102 areas, 18 cells for α5-GFP on poly-D-lysine, and 137 areas, 30 cells for α5-GFP on fibronectin. The DA values were calculated from the spatial correlation function x-axis fit because the GAP-GFP was moving during the time the laser beam moved from one row of the image to the next. For consistency the integrin DA values were also calculated from the x-axis fit. The DA of 6.02±0.07 for GAP-GFP was used to normalize the data and calculate the number of proteins per cluster for α5-integrin. The break for low and high expressers was set at an average intensity of below or above 300 intensity units. Error bars are s.e.m. Scale bars, 5 μm.

de-clustering of adhesion components. To identify mechanisms that may traffic molecules out of these regions and characterize changes in integrin organization, image sequences were analyzed by ICM to calculate diffusion coefficients, flow rates and immobile fractions of integrins from the measured temporal correlation functions (see Materials and Methods). When flow was present a directional correlation analysis was done to determine the magnitude and net direction of directed integrin transport (see Materials and Methods). These analyses provided maps of protein dynamics across the cell and enabled us to compare dynamic regions of the cell with quiescent ones.

Temporal ICM was used to produce a spatial map of α5-integrin dynamics across a CHO-B2 cell (Fig. 5A and Movie 1 in supplementary material). The α5-integrin was essentially immobile in the central regions of the cell (regions 4 and 5, Table 1, $D_{\alpha5}$=0.04-0.11×10^{-11} cm^2 s^{-1}; 96-97% immobile), whereas there was a faster diffusive component in regions where protrusions were forming and retracting (regions 1 and 3, Table 1, $D_{\alpha5}$=2.4 and 0.5×10^{-11} cm^2 s^{-1}; 39% and 70% immobile, respectively). In region 1, where the cell protrudes and then retracts, α5 showed a significant, net directed movement towards the cell body (v =0.7±0.1 μm s^{-1}). In other regions, a small fraction of α5 was also undergoing directed movement (3-4%, v =1-2±0.3 μm s^{-1}); however, it was not detected by a

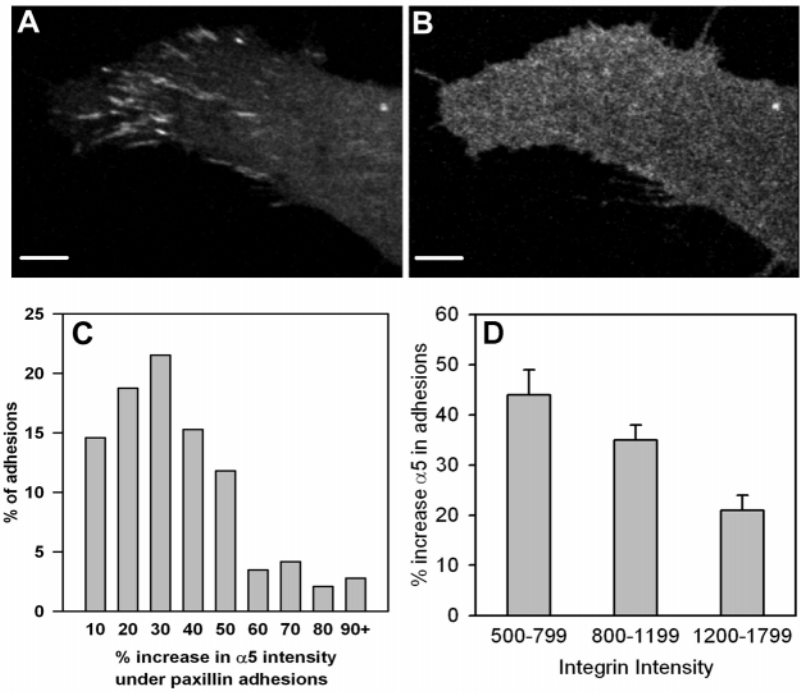

Fig. 3. Integrins are concentrated in nascent adhesions demarked by the presence of paxillin-containing adhesions. MEF or CHO cells were transfected with both paxillin-CFP (A) and α5-YFP (B). Confocal image time series were collected 24 hours after transfection and 1 hour after cells were plated on coverslips coated with 1 μg ml^{-1} fibronectin. The % increase in the intensity of α5-YFP in nascent adhesive areas relative to adjacent areas was calculated and plotted as a histogram (C; 144 adhesions, 17 cells). In 5% of the adhesions measured, α5-integrin showed an equal or slightly lower intensity of fluorescence in areas adjacent to paxillin containing adhesions. (D) The relative concentration of α5-integrin in adhesive areas is higher for lower-expressing cells. For the two image frames shown there is a 27% increase in α5 intensity under paxillin based on measurements taken on 20 adhesions. Scale bar, 5 μm.

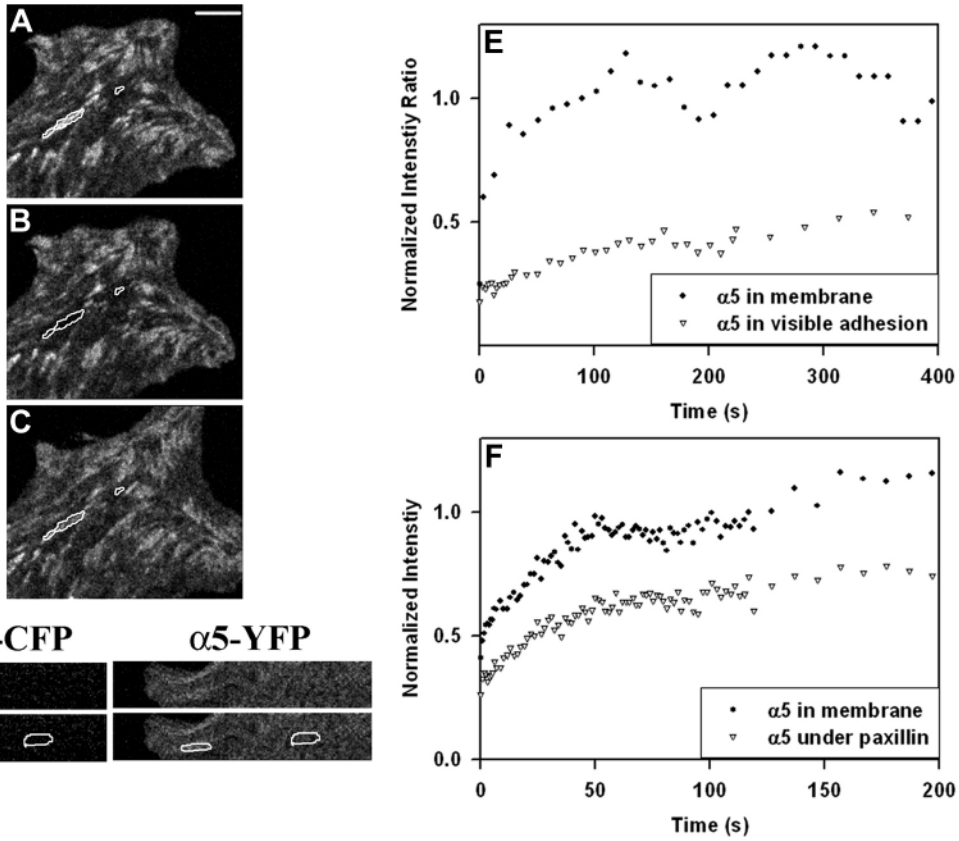

Fig. 4. FRAP of α5-integrin shows that it is less mobile in adhesive regions of the cell. Confocal images of α5-GFP expressed in a CHO B2 cell plated on 2 μg ml^{-1} fibronectin for 3 hours at 37°C. The first image in the time series (A), the first image after bleaching (B) and the last image (C) in the time series are shown. (D) MEF cells transfected with paxillin-CFP and α5-YFP about 1 hour after plating on 1 μg ml^{-1} fibronectin. The lower panel shows where the α5-YFP was bleached both under paxillin and in a more central area of the cell. The paxillin-CFP was not bleached. Normalized FRAP curves showing the recovery of α5-GFP from the highlighted regions in A-C (E) or of α5-YFP (F) from the highlighted regions in D. The plots show the normalized intensity of fluorescence following bleaching of organized (open triangles) or nonorganized α5-integrin (filled circles) in either case. Scale bar, 5 μm.

directional correlation analysis and therefore the movement was directionally random (regions 4 and 5, Fig. 5A, Table 1).

Changes in integrin dynamics and density during adhesion disassembly

Fig. 6A,B shows the first and last frames from a confocal image time series with near complete dispersion of visible α5-integrin containing adhesions (see boxed region, Movie 2 in supplementary material). An ICM analysis of the region just below where the adhesions are disassembling shows a measurable diffusion coefficient ($D_{\alpha5}=0.7\times10^{-11}$ cm^2 s^{-1}, 48% mobile), whereas other areas of the cell that were analyzed show that the integrin is essentially immobile ($D<10^{-12}$ cm^2 s^{-1}, not shown). A randomly directed, nondiffusive component, probably due to vesicular traffic, is also present.

Changes in the density of the α5-integrin in individual adhesions during adhesion disassembly were quantified by measuring the fluorescence intensity relative to GAP-GFP. The intensity measurements on individual adhesions in region 1 show that the integrin density decreases from ~875 to ~365 α5-integrins μm^{-2} as the bright adhesions disassemble; this corresponds to a two-to-threefold decrease in integrin density (adhesions 1-4 Fig. 6E, filled circles Fig. 6C, Table 2). For comparison, there was little change in integrin density in nonadhesive areas over the same time interval (area 8 Fig. 6E, open triangles Fig. 6C, Table 2). This change in integrin density was relatively modest, suggesting that changes in organization (clustering) might also be important. Following adhesion disassembly, the density of integrins did not reach nonadhesive values but remained ~1.7 times higher (Fig. 6C, Table 2). This probably reflects residual immobile integrin clusters remaining as footprints on the substratum (Laukaitis et al., 2001). From an exponential fit of the time decay of the integrin density (Fig. 6C), the half-time for disassembly of α5-integrin was 6.3±0.7 minutes (k=0.16±0.02 min^{-1}), which is consistent with data on paxillin adhesion disassembly kinetics (Webb et al., 2004).

Dynamics of α-actinin and paxillin during adhesion disassembly

For comparison with the α5-integrin, we used ICM to map the dynamics of α-actinin (Fig. 5B, Table 3), a cytoplasmic adhesion component implicated in the linkage between integrins and the actin cytoskeletal network (Brakebusch and Fassler, 2003). As with the α5-integrin, the α-actinin mobility was spatially heterogeneous. In peripheral, protruding regions (see Movie 3 in supplementary material), α-actinin was highly mobile with a small immobile fraction (30% immobile, regions 6 and 15, $D_{\alpha\text{-actinin}}=1.88\pm0.08$ and $3\pm1\times10^{-11}$ cm^2 s^{-1}, respectively). In the highly active regions of the cell periphery where the cell was extending protrusions, ruffling or retracting, a significant fraction of the α-actinin molecules were also undergoing directed movement at a net rate of 0.2–0.25 μm min^{-1} (20-30% immobile, regions 5, 15 and 16), a value similar to that reported for retrograde flow of cortical actin in these regions (Vallotton et al., 2003). In more central quiescent regions of the cell the diffusion coefficients were lower (regions 8 and 10, $D_{\alpha\text{-actinin}}=0.4\pm0.1$ and $<0.1\times10^{-11}$ cm^2 s^{-1}, respectively), and a large percentage of the protein was immobile (80%, regions 9 and 11).

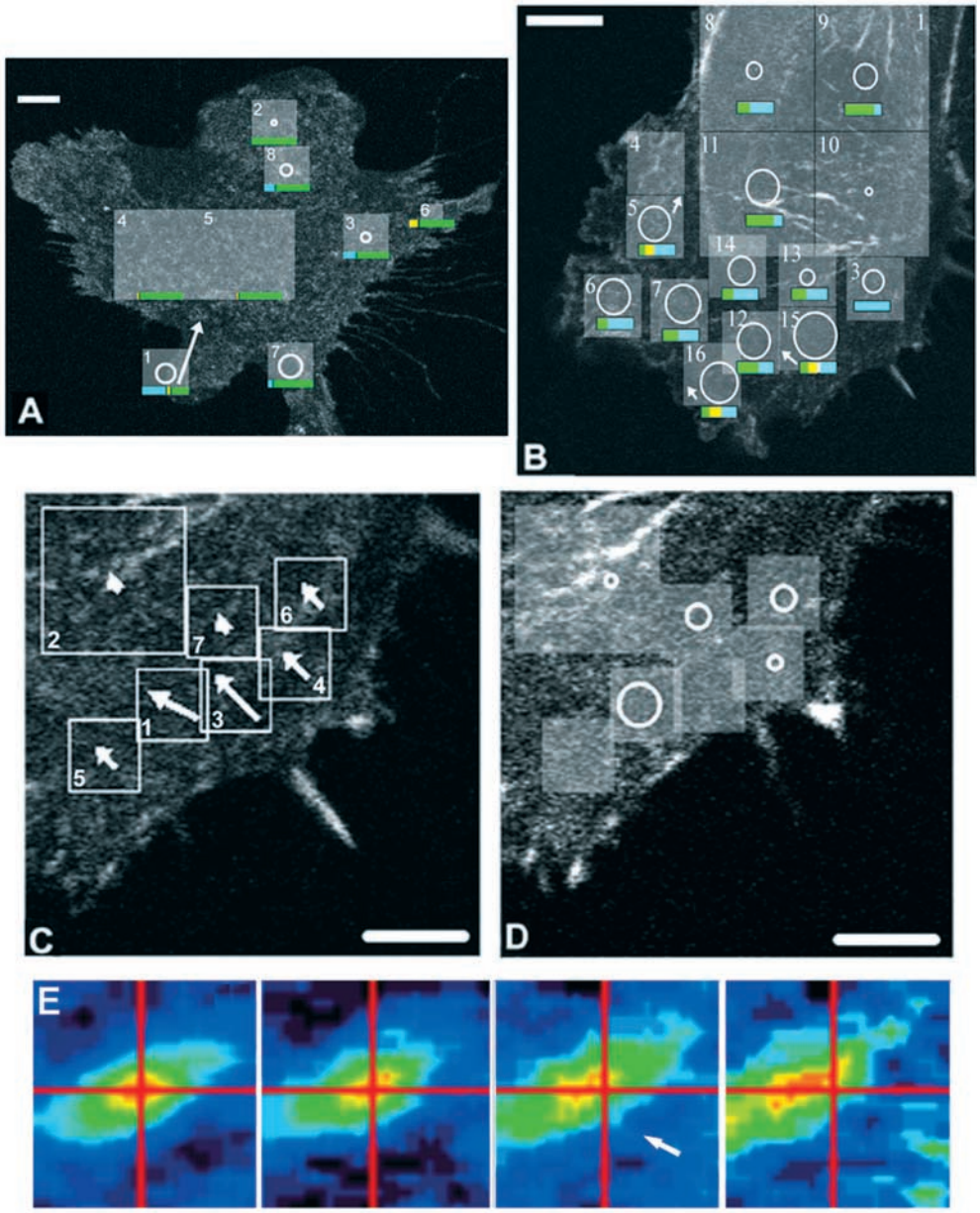

Fig. 5. A spatial map of the dynamics of α5-integrin or α-actinin across the cell. ICM results for a confocal image time series of α5-GFP expressed in a CHO-B2 cell plated for 1 hour on 2 μg ml^{-1} fibronectin (A), or for a two-photon microscopy image time series of α-actinin-GFP on a CHO-B2 cell plated for 24 hours on 5 μg ml^{-1} fibronectin (B), (C) and (D). Both image series were collected at 37°C. A temporal ICM analysis was performed on each of the highlighted regions of size 128^2, 64^2 or 32^2 pixels. Image stacks were with 100 frames at 0.111 μm (A) or 0.118 μm (C,D) pixel size and a frame interval of 5 seconds. The temporal correlation functions were fit to Equations 11, 12 and 13 and the fit with the best R^2 value was used. The circles represent the root mean square average diffusion distance from the center of the circle for a 10 minute period based on the measured average diffusion coefficient for each region. The vectors represent the mean translation distance and direction over a 10 minute period based on the measured velocities for regions exhibiting flowing integrin populations. The colored bars depict the proportion of immobile (green), flowing (yellow) and diffusing (cyan) integrin or α-actinin within each region. For the α5-GFP image series some areas appear to be off of the cell (e.g. area 1). If this was the case the analysis was limited to the image frames where the region of interest was completely on the cell. Region 6 was too small for the directional correlation analysis. Correlation velocity mapping was done for small areas around a retracting microspike just below region 3 in Fig. 5B. The arrows show the direction of the flow component of the correlation function and the size of the arrow is proportional to the magnitude of the velocity in that area of the cell. (D) Correlation analysis of images 70-100 of the image time series showing diffusion of α-actinin after adhesion disassembly. (E) Spatial-temporal correlation functions for α-actinin in area 1 shown in Fig. 5C. Notice the center of the correlation function peak moves from the center of the axis in the direction shown by the arrow as things flow towards the upper left quadrant. Scale bars, 5 μm (A,C,D) or 10 μm (B).

Table 1. Measured temporal and spatial ICM parameters for α5-integrin on image regions of a CHO B2 cell expressing α5-integrin-GFP

Region	D×10^{-11} (cm^2 s^{-1})	|v| (μm min^{-1})	Diffusing (%)	Flowing (%)	Immobile (%)	<DA>
1	2.4±0.4	0.7±0.1	53±5	7±2	39±3	7
2	0.14±0.02	–	–	–	100±6*	6
3	0.5±0.2	–	30±5	–	70±8	3
4	0.11±0.02	1.7±0.3	–	4±1	96±10*	6
5	0.04±0.02	0.9±0.2	–	3±1	97±59*	6
6	–	0.58±0.04	–	20±1	80±1	6
7	3±1	–	13±1	–	87±2	6
8	0.7±0.4	–	23±6	–	77±9	7

*These areas show diffusion but the rate is so slow it is considered essentially immobile. See also Fig. 5A. Diffusion coefficients, flow speeds, and percentage of protein within each protein population are given for diffusing, flowing, and immobile integrin populations in given regions of interest. The DA normalized versus GAP-GFP for the first image in the time series is also shown.

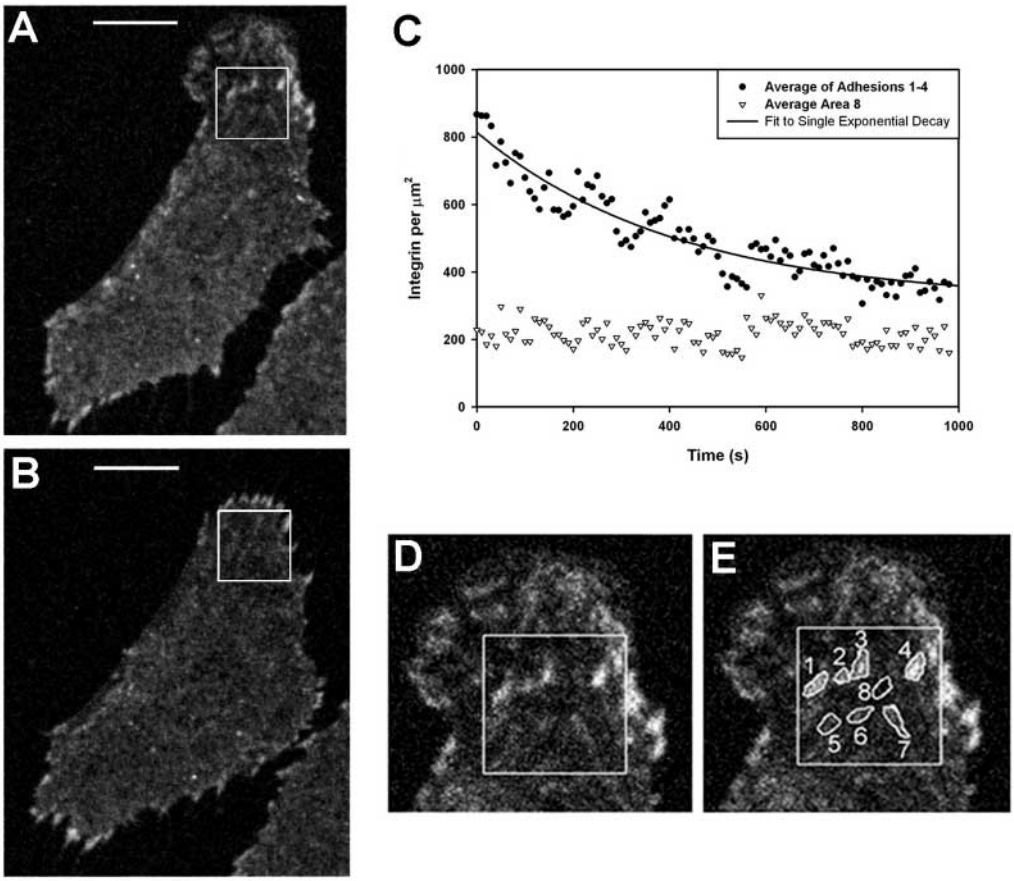

Fig. 6. Disassembly of α5-integrin in a retracting region of the cell. Confocal images of CHO B2 cells stably expressing α5-GFP 3 hours after plating on 2 μg ml^{-1} fibronectin. The first (A) and the last image in the 17 minute time series (B) are shown. Plots of the average intensity of the four bright adhesions (filled circles) and of a nonadhesive area (open triangles, region 8) within the boxed region are shown. A single exponential fit was made to the data to determine the rate of adhesion disassembly. (D,E) Outlines of individual adhesions from the boxed region that were analyzed by intensity to provide a measure of integrin density within adhesions (Table 2). Scale bars, 10 μm.

In the lower right area of the image shown in Fig. 5B, α-actinin is present in an adhesion that disassembles (Fig. 5C, Movie 3 in supplementary material). A directional correlation analysis of the dynamics of α-actinin in the vicinity of the disassembling adhesion shows that α-actinin executes a net flow away from the adhesion towards the center of the cell. The fastest net flow, 0.29 μm min^{-1}, occurs at the base of the adhesion (Fig. 5C, region 3, Table 4). This rate corresponds to the rate of filamentous actin retrograde flow (Vallotton et al., 2003), suggesting that an analogous actin dynamic may occur in regions where adhesions disassemble. Fig. 5E shows the spatial-temporal correlation peak for region 1 (Fig. 5C), and the arrow highlights the peak movement from the zero lag position (marked by the intersection of the red lines) in the direction of flow. Interestingly, shortly after adhesion disassembly and retraction, the inward flow terminates, and the α-actinin in the region undergoes simple diffusive movement ($D_{\alpha\text{-actinin}}=0.13 - 2.6\times10^{-11}$ cm^2 s^{-1}, Fig. 5D, Table 4).

The dynamics of paxillin differ from that of both integrin and α-actinin. No diffusive, flowing or immobile populations of paxillin in nonadhesive areas or in areas near adhesions that are undergoing disassembly was observed. FRAP analyses show that the diffusion of paxillin in these regions is much faster than that of either integrin or α-actinin and is too fast to

Table 2. Calculated number of integrins per adhesion from the region highlighted in Fig. 6A based on measured area of the adhesion and the intensity of the adhesion relative to the intensity of GAP-GFP

	First frame of movie		Last frame of movie		
Adhesion (see Fig. 6E)	Integrins μm^{-2}	Protein relative to nonadhesive area	Integrins μm^{-2}	Protein relative to nonadhesive area	Factor change in density
1	910±20	5	340±10	1.6	2.6
2	740±20	4	240±10	1.1	3.1
3	720±10	4	380±10	1.8	1.9
4	1130±20	6	500±10	2.4*	2.2
5	410±10	2	300±10	1.4	1.3
6	460±10	2	370±10	1.7	1.3
7	530±10	3	350±10	1.7	1.5
8	190±10	1	210±10	1.0	0.1

*This corresponds to the minimum value for this adhesion but it began to grow when the cell retracted so it does not correspond to the last frame of the movie. It was assumed that GAP-GFP was monomeric in order to determine the number of proteins per adhesion. A measured beam radius of 0.31 μm from GAP-GFP autocorrelation function fits was used in the calculations. Data was also corrected for differences in laser power between the GAP-GFP measurements and these measurements. Error measurements are s.e.m.

Table 3. Measured temporal and spatial ICM parameters for α-actinin on regions of a CHO B2 cell

Region	$D\times10^{-11}$ ($cm^2\ s^{-1}$)	$<N>_{diffusing}$ (μm^{-2})	$\lvert v\rvert$ ($\mu m\ min^{-1}$)	$<N>_{flowing}$ (μm^{-2})	$<N>_{immobile}$ (μm^{-2})	<DA>
3	0.78±0.08	6.9±0.7	–	–	–	1.7
5	1.8±0.8	8±3	0.23±0.08	3±1	3±2	1.7
6	1.88±0.08	2.1±0.7	–	–	0.82±0.03	6.2
7	2.1±0.2	4.2±0.2	–	–	3.3±0.2	2.2
8	0.4±0.1	0.8±0.2	–	–	0.4±0.2	7.8
9	0.94±0.05	0.33±0.01	–	–	1.35±0.03	5.4
10	<0.1	–	–	–	–	–
11	1.9±0.1	0.34±0.01	–	–	1.05±0.03	5.0
12	1.8±0.2	2.3±0.1	-	-	3.2±0.2	1.9
13	0.38±0.02	4.8±0.2	-	-	3.4±0.2	5.3
14	1.23±0.09	9.9±0.5	–	–	4.2±0.3	1.4
15	3±1	9±2	0.25±0.1	5±1	6±2	0.9
16	2±1	2±1	0.20±0.04	1.4±1.2	1±1	1.6

See also Fig. 5B. Diffusion coefficients, flow speeds, and number densities per unit area squared are given for diffusing, flowing, and immobile integrin populations in given regions of interest. The DA for the first image in the time series is also shown. Note that these DA values are calculated from two photon images and do not correspond to the GAP-GFP normalized values.

Table 4. Measured temporal ICM parameters for α-actinin on regions of a CHO B2 cell expressing α-actinin-GFP near a disassembling adhesion

	First 70 frames			Last 30 frames	
Region	$D\times10^{-11}$* ($cm^2\ s^{-1}$)	$\lvert v\rvert$* ($\mu m\ min^{-1}$)	Immobile* (%)	$D\times10^{-11}$ † ($cm^2\ s^{-1}$)	Immobile† (%)
1	6±2	0.25±0.06	28	2.6±0.8	64
2	1.7±0.5	0.10±0.03	13	0.13±0.04	0
3	3.1±0.9	0.29±0.01	0	–	50
4	1.8±0.5	0.18±0.02	0	0.21±0.06	0
5	0.8±0.2	0.15±0.03	15	–	50
6	1.1±0.3	0.16±0.05	41	0.6±0.2	0
7	0.6±0.2	0.11±0.01	6	0.6±0.2	6

*, values for first 70 frames of movie. †, values for last 30 frames of movie. See also Fig. 5C,D. Diffusion coefficients, flow speeds and percentage of immobile protein are given for the given regions of interest.

be captured with the time resolution of these ICM measurements (not shown). By contrast, FRAP analyses show that most of the α-actinin and α5-integrin are not free in the cytoplasm or membrane, respectively, but rather associated with some structure that inhibits its rapid diffusion as a free molecule (not shown).

Thus, as adhesions disassemble we see distinct fates for three different adhesion components. The α5-integrin diffuses away or is left on the substratum, α-actinin moves away directionally and paxillin diffuses away rapidly presumably into the cytosolic volume. This is consistent with previous studies that have provided evidence for a decoupling of integrin and the cytoskeleton in retracting regions with the integrin remaining on the substrate and cytoskeletal components like α-actinin detaching from integrin and retracting toward the cell body (Laukaitis et al., 2001; Webb et al., 2002). The present analyses extend these observations by examining the fates of components during adhesion disassembly and quantifying their transport rates.

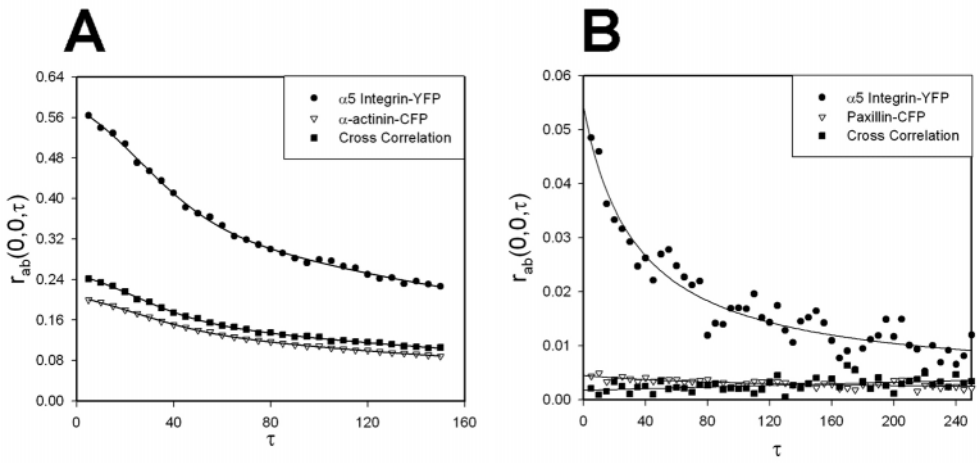

Fig. 7. Temporal ICCM Correlation Functions for α5-integrin-YFP correlated with α-actinin-CFP or paxillin-CFP. Temporal ICCM correlation functions were calculated from two-photon microscope image time series of CHO B2 cells expressing α5-integrin-YFP and α-actinin-CFP (A) or α5-integrin-YFP and paxillin-CFP (B). The integrin-paxillin data were calculated from images in a central region of the cell where there was no organized paxillin. The temporal integrin autocorrelation function (closed circles), α-actinin or paxillin autocorrelation function (open triangles) and the cross-correlation function (closed squares) are shown. Cross-correlation functions and the YFP autocorrelation function were corrected for bleed through of the CFP signal into the YFP channel (see Materials and Methods).

α5-integrin and α-actinin diffuse and flow as a complex

Our observation that integrins are

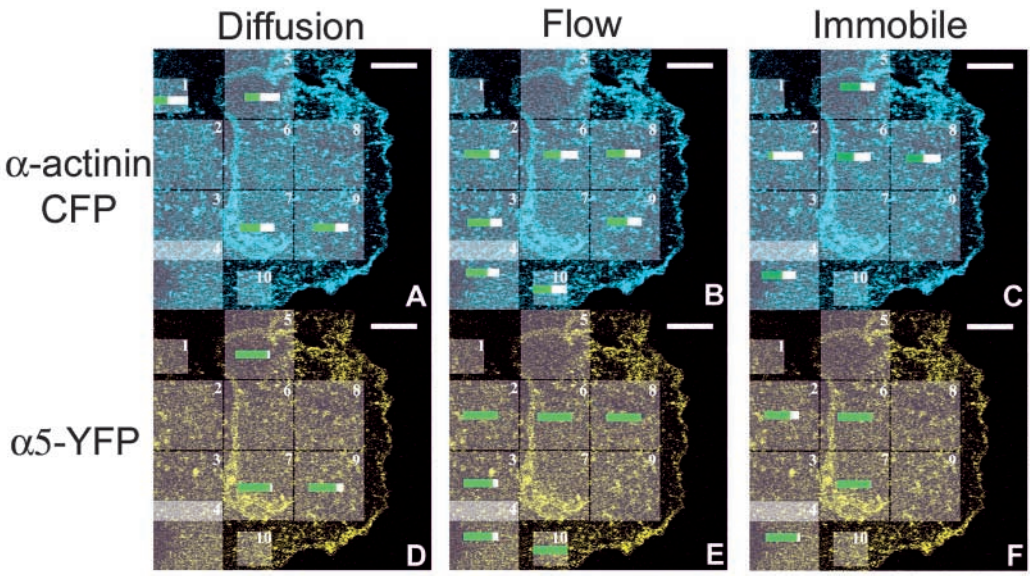

Fig. 8. ICCM analysis of α5-YFP and α-actinin-CFP. Two-photon fluorescence microscopy images collected at 37°C of α-actinin-CFP (A-C) and α5-YFP (D-F) 2.5 hours after plating on 10 μg ml^{-1} fibronectin. ICM and ICCM were conducted on each highlighted region of the cell. The distribution of α-actinin, α5-integrin or colocalized species was determined via spatial autocorrelation or cross-correlation analysis. The dynamics of α-actinin, α5-integrin or complexes moving together was determined via a temporal autocorrelation or cross-correlation analysis. Spatial functions were fit to Equation 4, and temporal functions were fit to one of Equations 11, 12 or 13. Equation 17 was used to estimate the fraction of each population that was immobile. The green bars show the fraction of a given species (diffusing, flowing or immobile) that is interacting with the second fluorescently tagged protein within a complex. The white part of the bar is the fraction noninteracting – i.e. the green bar in a region of the cell in Fig. 8A would represent the fraction of α-actinin that is diffusing together with α5-integrin, whereas the green bar in Fig. 8D would represent the fraction of α5-integrin that is diffusing together with α-actinin. Similarly, the green bar in Fig. 8B and 8E show the fractions of the respective proteins that are flowing together, and Fig. 8C and 8F represent the fraction of each protein population that is immobile and colocalized. Scale bars, 10 μm.

clustered in regions that are not discernibly organized suggests that they may reside in small, submicroscopic complexes that include other adhesion molecules. To investigate this, image cross-correlation microscopy (ICCM) was used to assay for associations between α5-integrin and α-actinin or paxillin (Wiseman et al., 2000). In ICCM, spatial or temporal intensity fluctuations from two different fluorescent molecules (such as CFP and YFP) were analyzed by computing the cross-correlation function between two images. A non-zero spatial cross-correlation shows that the proteins reside together in a common complex, and a non-zero temporal cross-correlation function shows that they move together as a complex (Fig. 7A; see Materials and Methods).

The temporal ICCM data show that α5-integrin-YFP and α-actinin-CFP reside in a complex, i.e. they have a non-zero cross-correlation function (Fig. 7A; filled squares), which has immobile, diffusing and flowing populations (Fig. 7A; Fig. 8A-F). In addition to detecting the distribution and dynamics of protein complexes, this analysis also allowed the calculation of the percentage of each protein population that is interacting in the complex (Table 5, Fig. 8). For example, in region 7, almost all of the diffusing population of α5-integrin was diffusing with α-actinin (Fig. 8D; Table 5), and a significant, but lower faction, of the α-actinin was diffusing with the integrin (Fig. 8A; Table 5). A population of α-actinin that is associated with actin and not integrin probably contributed to this difference. The presence of endogenous as well as ectopic α-actinin in these cells may have also contributed. Table 6 shows the dynamic parameters measured for the diffusing and flowing α5-integrin/α-actinin complexes for the various regions of the cell shown in Fig. 8. It is interesting that nearly all of the α5-integrin, throughout the cell, whether immobile, flowing or diffusing is associated with α-actinin (Fig. 8D-F), including regions of the cell that do not contain any organized integrin or α-actinin. This suggests that integrin is associated with α-actinin even before it is visibly organized in large adhesions.

By contrast, interactions between paxillin and α5-integrin were not detected in regions outside of adhesions. This is shown by the zero value for the cross-correlation function between α5-integrin-YFP and paxillin-CFP (Fig. 7B, filled squares). However, interactions were detected between paxillin and α5-integrin in regions of the cell that have organized adhesions (not shown).

Discussion

Elucidating the mechanisms by which adhesions form and disassemble is an increasingly timely but persistently elusive challenge. Questions include: what is the organization of nascent adhesions? How does the organization of adhesions change as they assemble and disassemble? What are the fates of adhesion components following adhesion disassembly? Do adhesion components reside in complexes outside of adhesions? Because these processes are spatially restricted, carefully regulated and highly dynamic, it is becoming increasingly clear that progress in this area will be accelerated by the development of new imaging modalities.

In this study we have addressed the organization and dynamics of integrins in adhesions on migrating cells using correlation microscopy. In its usual rendition, fluorescence correlation spectroscopy (FCS), a small focal region of the cell is illuminated, and by correlation analysis of the temporal fluctuations in fluorescence intensity, the concentration, aggregation state and dynamics of a fluorescently tagged component are determined (Elson and Magde, 1974). When two different molecules are tagged with different fluorophores, cross-correlation analyses provide estimates of the dynamics, concentration and interactions of any molecular complexes that

Table 5. Measured temporal ICCM parameters for α5-integrin and α-actinin on image regions of a CHO B2 cell

	α-actinin			α5-integrin		
Region	Co-diffusing (%)	Co-flowing (%)	Immobile-co-localized (%)	Co-diffusing (%)	Co-flowing (%)	Immobile-co-localized (%)
1	40±2	–	–	114±4	–	–
2	–	76±8*	14±2	–	107±9	75±11
3	–	65±5*	–	–	84±7	–
4	–	66±5†	62±2	–	82±5	92±3
5	42±2	–	58±3	92±2	–	–
6	–	51±5†	–	–	101±7	112±18
7	56±3†	–	–	100±4		99±9
8	–	56±3†	50±6	–	100±4	–
9	63±12	60±16	–	80±11	–	–
10	–	56±8†	–	–	109±13	–

*One protein population that is both diffusing and flowing. †Two protein populations, one that is diffusing and one that is flowing. See Fig. 8A-F. Percent of protein populations that are co-diffusing, co-flowing or immobile and co-localized for the regions shown in Fig. 8. Percentages were calculated using the ICM and ICCM data and Equation 17.

Table 6. Measured dynamics from a temporal ICCM analysis of α5-integrin and α-actinin from regions of a CHO B2 cell

Region	Integrin/α-actinin complex $D\times10^{-11}$ ($cm^2\ s^{-1}$)	Integrin/α-actinin complex $\|v\|$ ($\mu m\ min^{-1}$)
1	1.4±0.2	–
2*	1.7±0.2	0.50±0.10
3*	1.3±0.1	0.40±0.07
4*	1.6±0.3	0.64±0.05
5	4.0±0.4	–
6*	2.0±0.2	0.59±0.07
7	1.9±0.1	–
8*	1.0±0.1	0.60±0.03
9†	0.8±0.4	1.01±0.07
10*	1.0±0.2	0.4±0.1

*One protein population that is both diffusing and flowing. †Two protein populations, one that is diffusing and one that is flowing. See Fig. 8A-F. Data were fit with one of Equations 11-13 and the fit with the best R^2 value was chosen.

include both molecules (FCCS) (Bacia and Schwille, 2003). Image correlation microscopy [ICM; alternatively called image correlation spectroscopy (ICS)] is a variant technology that analyzes spatial intensity fluctuations from images obtained by laser scanning confocal microscopy (Petersen et al., 1993). Previously, it had been used primarily to determine the concentration, aggregation and interactions of molecules on fixed cells (Petersen et al., 1998, Wiseman et al., 2000). In the present study, we have greatly extended this technology to retrospectively analyze image time series (retrospective image correlation) from migrating cells and provide spatial maps of the concentration, aggregation state, interactions and transport properties of integrins in migrating cells. We have also used ICM to calibrate fluorescence intensities to provide estimates of the molecular density of integrins in adhesions and used directional correlation analyses to determine the net direction and magnitude of nonrandom movements. These analyses have provided novel insights into integrin and adhesion organization and dynamics in migrating cells.

Previous studies have shown that under migration promoting conditions, integrins are not highly organized, in contrast to the readily discernible organization of other adhesion components like paxillin (Laukaitis et al., 2001). We have found that integrins in cells plated on fibronectin, even though they are not discernibly organized, reside in small clusters that average three to four integrins. This average value includes any unclustered integrin; thus it is probably underestimating the size of any clusters per se. Consistent with this, the average integrin cluster size is lower in cells expressing higher levels of integrin. This suggests that the integrin cluster size is determined by a fixed number of intrinsic sites that are saturated at relatively low levels of integrin expression. This idea is also supported by the fact that the relative density of integrin in nascent paxillin containing adhesions increases at lower expression levels.

The notion that integrins are organized in submicroscopic clusters is supported by three other observations. First, the diffusion coefficients determined by either FRAP or ICM are much slower than that for freely diffusing membrane proteins, which is consistent with a transient linkage to a relatively immobile structure. Second, FRAP analyses show that 32% of the integrins in nascent paxillin containing adhesions are immobile, in contrast to the nearly complete mobility of the integrins outside adhesions. Third, using paxillin as a marker, our data show that α5-integrin is 1.3–2 times more concentrated and ~4.5 times more clustered in nascent adhesions than in surrounding regions. These three observations are all consistent with the hypothesis that new adhesions are nucleated by relatively small integrin clusters.

Previous analyses of disassembling adhesions in retracting regions of the cell have shown that a portion of the integrins remains on the substratum while the cytoplasmic components, as a whole, tend to slide toward the center of the cell and/or ‘disperse’. The ICM data provide insights into these adhesions and the disassembly process. The density of integrins in the more mature adhesions in retracting regions differs from those of nascent adhesions. The former is two-to-sixfold higher than surrounding regions, while the later is only 1.3-2-fold higher. These relative densities correspond well with those measured on β3-integrin (Ballestrem et al., 2001), and we have extended their analysis by estimating the number of integrins in adhesions. The bright adhesions have a density of between 700 and 1200 integrins μm^{-2}, whereas the dimmer adhesions have 400-600 integrins μm^{-2}. This is compared with 50-390 integrins μm^{-2} in nonorganized regions of the cell (the large range of densities represents highly variable expression levels). The integrin adhesion disassembly is incomplete, consistent

with a portion of the integrin remaining attached to the substratum (Laukaitis et al., 2001), and the rate of disassembly of the integrins that do move out of adhesions corresponds well with rates of disassembly of paxillin (Webb et al., 2004).

The dynamics of integrin, α-actinin and paxillin in the vicinity of the disassembling adhesions differ dramatically. Many of the integrins diffuse away relatively slowly, some not at all. By contrast, α-actinin undergoes a net directed movement away from the adhesion that ceases after the adhesion disassembles. The rate of this movement is similar to that reported for retrograde flow suggesting that an analogous mechanism might be involved and a potential contractile coupling between the retraction and disassembly of the adhesion. This movement differs from the sliding of the adhesion, per se, as it is seen in regions where the α-actinin is not visibly organized. The α-actinin in these regions is probably not coupled to integrin as there is no evidence for a similar, robust net transport of integrin in retracting regions. Some integrins near disassembling adhesions undergo nondiffusive movements that do not show a net directed transport; however, this probably reflects vesicles that are moving about in the vicinity of the adhesions. Finally, paxillin appears to leave adhesions rapidly without any apparent connection to either α-actinin or integrin.

The robust interaction between α-actinin and integrins outside of adhesions, as revealed by ICCM, provides direct evidence for the presence of integrin in complexes throughout the cell surface. Immobile, diffusing and flowing populations of integrins all interact with α-actinin. The ICCM analyses do not reveal whether or not the interactions between α5-integrin and α-actinin are direct and thus raise the interesting possibility that other components may reside in these complexes as well. It is interesting that both integrin and α-actinin are present prominently at the leading edge of the cell, suggesting the possibility that they also co-reside there in complexes. However, as adhesions form near the leading edge, these complexes probably change given that colocalization studies do not reveal an interaction between α-actinin and integrin in nascent adhesions (von Wichert et al., 2003). These clusters could reflect either very small, submicroscopic adhesions, vesicles, or more probably, preformed complexes of select adhesion components that are diffusing and trafficking throughout the cell.

While our studies have provided significant insight into adhesion organization and dynamics, the power of ICM, ICCM and other correlation microscopy techniques has only begun to be exploited for analyses of cellular processes involving spatial and temporal changes in participating molecules. The technology promises to provide spatial and temporal maps of the concentrations, diffusion rates, directed movements, degree of aggregation and interactions among cellular components. It also promises to help parse the plethora of potential interactions that characterize many signaling processes and other complex biological phenomena. In addition, the quantitative data derived from these analyses will be useful for modeling cellular phenomena by providing concentrations, interactions and rate information. Finally, these technologies will be useful for analyzing cells and regions of cells that are organized on a submicron scale. The ability to analyze images retrospectively also has important implications for the development of high-throughput cellular screens and assays. Thus, ICM and ICCM are exciting, important and timely additions to the emerging arsenal of technologies for studying complex, polarized processes like cell migration, signal transduction, adhesion, cytoskeletal organization, mitosis and cytokinesis.

P.W.W. was funded by the LJIS Interdisciplinary Training Program, the Burroughs Wellcome Fund, and the Natural Sciences and Engineering Research Council of Canada (NSERC), the National Center for Microscopy and Imaging Research (NCMIR-NIH award #P41-RR04050, microscope designed by R. Y. Tsien in collaboration with Nikon Corp. (Japan), BioRad Laboratories), and NSF grant DBI-9987257 (JAS). A.F.H. was supported by NIH grant GM23244 and the Cell Migration Consortium, NIGMS U54 GM064346. D.J.W. was supported by NIH postdoctoral training grant HD07528. Thank you to X. Asay-Davis and T. Foley for programming assistance, James Bouwer for general assistance with the RTS 2000 microscope and D. Kolin for assistance with the transport analysis.

References

Bacia, K. and Schwille, P. (2003). A dynamic view of cellular processes by in vivo fluorescence auto- and cross-correlation spectroscopy. *Methods* **29**, 74-85.

Ballestrem, C., Hinz, B., Imhof, B. A. and Wehrle-Haller, B. (2001). Marching at the front and dragging behind: differential alphaVbeta3-integrin turnover regulates focal adhesion behavior. *J. Cell Biol.* **155**, 1319-1332.

Brakebusch, C. and Fassler, R. (2003). The integrin-actin connection, an eternal love affair. *EMBO J.* **22**, 2324-2333.

Del Pozo, M. A., Kiosses, W. B., Alderson, N. B., Meller, N., Hahn, K. M. and Schwartz, M. A. (2002). Integrins regulate GTP-Rac localized effector interactions through dissociation of Rho-GDI. *Nat. Cell Biol.* **4**, 232-239.

Elson, E. L. and Magde, D. (1974). Fluorescence correlation spectroscopy. I. Conceptual basis and theory. *Biopolymers* **13**, 1-27.

Fan, G. Y., Fujisaki, H., Miyawaki, A., Tsay, R. K., Tsien, R. Y. and Ellisman, M. H. (1999). Video-rate scanning two-photon excitation fluorescence microscopy and ratio imaging with cameleons. *Biophys. J.* **76**, 2412-2420.

Horwitz, A. R. and Parsons, J. T. (1999). Cell migration–movin' on. *Science* **286**, 1102-1103.

Lauffenburger, D. A. and Horwitz, A. F. (1996). Cell migration: a physically integrated molecular process. *Cell* **84**, 359-369.

Laukaitis, C. M., Webb, D. J., Donais, K. and Horwitz, A. F. (2001). Differential dynamics of alpha 5 integrin, paxillin, and alpha-actinin during formation and disassembly of adhesions in migrating cells. *J. Cell Biol.* **153**, 1427-1440.

Liu, Y., Fisher, D. A. and Storm, D. R. (1993). Analysis of the palmitoylation and membrane targeting domain of neuromodulin (GAP-43) by site-specific mutagenesis. *Biochemistry* **32**, 10714-10719.

Neff, N. T., Lowrey, C., Decker, C., Tovar, A., Damsky, C., Buck, C. and Horwitz, A. F. (1982). A monoclonal antibody detaches embryonic skeletal muscle from extracellular matrices. *J. Cell Biol.* **95**, 654-666.

Petersen, N. O. (1986). Scanning fluorescence correlation spectroscopy. I. Theory and simulation of aggregation measurements. *Biophys. J.* **49**, 809-815.

Petersen, N. O., Hoddelius, P. L., Wiseman, P. W., Seger, O. and Magnusson, K. E. (1993). Quantitation of membrane receptor distributions by image correlation spectroscopy: concept and application. *Biophys. J.* **65**, 1135-1146.

Petersen, N. O., Brown, C., Kaminski, A., Rocheleau, J., Srivastava, M. and Wiseman, P. W. (1998). Analysis of membrane protein cluster densities and sizes in situ by image correlation spectroscopy. *Faraday Discuss* **111**, 289-305.

Ridley, A. J., Schwartz, M. A., Burridge, K., Firtel, R. A., Ginsberg, M. H., Borisy, G., Parsons, J. T. and Horwitz, A. R. (2003). Cell migration: integrating signals from front to back. *Science* **302**, 1704-1709.

Schreiner, C., Fisher, M., Hussein, S. and Juliano, R. L. (1991). Increased tumorigenicity of fibronectin receptor deficient Chinese hamster ovary cell variants. *Cancer Res.* **51**, 1738-1740.

Thompson, N. L. (1991). Fluorescence correlation spectroscopy. In *Topics in Fluorescence Spectroscopy*, Vol. 1 (ed. J. R. Lakowicz), pp. 337-378. New York, NY: Plenum Press.

Vallotton, P., Ponti, A., Waterman-Storer, C. M., Salmon, E. D. and Danuser, G. (2003). Recovery, visualization, and analysis of actin and tubulin polymer flow in live cells: a fluorescent speckle microscopy study. *Biophys. J.* **85**, 1289-1306.

von Wichert, G., Haimovich, B., Feng, G. S. and Sheetz, M. P. (2003). Force-dependent integrin-cytoskeleton linkage formation requires downregulation of focal complex dynamics by Shp2. *EMBO J.* **22**, 5023-5035.

Webb, D. J., Parsons, J. T. and Horwitz, A. F. (2002). Adhesion assembly, disassembly and turnover in migrating cells – over and over and over again. *Nat. Cell Biol.* **4**, E97-E100.

Webb, D. J., Brown, C. M. and Horwitz, A. F. (2003). Illuminating adhesion complexes in migrating cells: moving toward a bright future. *Curr. Opin. Cell Biol.* **15**, 614-620.

Webb, D. J., Donais, K., Whitmore, L. A., Thomas, S. M., Turner, C. E., Parsons, J. T. and Horwitz, A. F. (2004). FAK-Src signalling through paxillin, ERK and MLCK regulates adhesion disassembly. *Nat. Cell Biol.* **6**, 154-161.

Wiseman, P. W. and Petersen, N. O. (1999). Image correlation spectroscopy. II. Optimization for ultrasensitive detection of preexisting platelet-derived growth factor-beta receptor oligomers on intact cells. *Biophys. J.* **76**, 963-977.

Wiseman, P. W., Squier, J. A., Ellisman, M. H. and Wilson, K. R. (2000). Two-photon image correlation spectroscopy and image cross-correlation spectroscopy. *J. Microsc.* **200**, 14-25.

Zacharias, D. A., Violin, J. D., Newton, A. C. and Tsien, R. Y. (2002). Partitioning of lipid-modified monomeric GFPs into membrane microdomains of live cells. *Science* **296**, 913-916.